Supporting Information

Structural and Defect Engineering of Cobaltosic Oxide Nanoarchitectures as Ultrahigh Energy Density and Super Durable Cathode for Zn-based Batteries

Chunlin Teng, Fan Yang, Minghui Sun, Keshu Yin, Qintong Huang, Guangying Fu, Chuanqi Zhang, Xihong Lu*, and Jiuxing Jiang*

Calculation

Special Capacity, energy density and power density

The specific capacity C_m (mAh g^{-1}) were calculated from the discharge curve using the following equations:

$$C_m = \frac{\int_0^{\Delta t} I \times dt}{m} \qquad \text{(Equation S1)}$$

Where I (mA) is the applied discharging current, Δt (h) is the discharging time and m (g) is the mass of active material.

The specific energy density E (Wh kg^{-1}) and power density P (W kg^{-1}) of the cell were obtained from the following equations:

$$E = C_m \times \Delta V \qquad \text{(Equation S2)}$$

$$P = \frac{E}{\Delta t} \qquad \text{(Equation S3)}$$

Where C_m is the specific capacity obtained from Equation (1) and ΔV (V) is working potential, and Δt (h) is the discharging time.

Electrochemically Active Surface Area (EASA)

The EASA for each system was estimated from the electrochemical double-layer capacitance of the electrode surface by CV method. The CV test at different scan rate in a potential range of 0.1 V where no apparent faradaic processes occur. The double-layer charging current i_c is equal to the product of the scan rate v, and the electrochemical double-layer capacitance C_{dl}, as given by equation S4:

$$i_c = v \, C_{dl} \qquad \text{(Equation S4)}$$

The anodic charging current (i) measured at one potential in CV curves as a function of the scan rate (v) for all electrodes. The slope of anodic charging current densities-scan rate curve is in direct equal to C_{dl}, which proportion to EASA.

$$EASA = \frac{C_{dl}}{C_s} \qquad \text{(Equation S5)}$$

Where C*s* is the specific capacitance measured for the sample with an atomically smooth planar surface, approximately 60 µF cm^{-2}.

Potentiostatic intermittent titration technique (PITT)

The ion diffusion for the PITT experiment can be modeled as one-dimensional transport based on Fick's second law (Equation S6):

$$\frac{\partial C_i}{\partial x} = D\frac{\partial^2 C_i}{\partial x^2}$$

(Equation S6)

Where x is the distance of ion moving from the electrolyte into the electrode, C_i is ion concentration at *x* and time *t*, and *D* is the chemical diffusion coefficient. In PITT measurement, a potentiostatic current transient was measured upon addition of a very small potential step (10 mV in this work). The transient current versus time can be approximately expressed as (Equation S7):

$$I(t) = \frac{2QD}{L^2}exp(-\frac{\pi^2Dt}{4L^2})$$

(Equation S7)

Where *Q* is the total charge transferred during a potential step and L is the thickness of the electrode (0.6 µm for our electrodes). The value of *D* can be calculated based on the logarithmic function of *I(t)* (equation S8):

$$D = -\frac{d\ ln(I)}{dt}\frac{4L^2}{\pi^2}$$

(Equation S8)

Density functional theory (DFT) calculation

The Vienna Ab-initio Software Package (VASP) is used to performed density functional theory (DFT). The interaction between the valence electrons and effects of core electrons are describe with the projector augmented wave (PAW) method. Generalized gradient approximation (GGA) with the Perdew-Burke-Ernzerhof (PBE) is some time used as the exchange and correlation energy. The plane wave is set to an energy of 600 eV. To model the surface of M-Co$_3$O$_4$ and oxygen-vacancy M-Co$_3$O$_{4-x}$, we use a (2×2) periodic slab models with four atomic layers combined with a 15 Å vacuum layer along the Z axis to eliminate the interaction between the slabs. The Monkhorst K-point grid of 5 × 5 × 1 grid was employed in the surface. In the slab calculations, the atoms in the top layer of the slab are allowed to relax and other bottom atoms are fixed. The atomic relaxation will be stop as soon as the energies within 1.0×10^{-5} eV/atom for total energy and the same the force on each atom is smaller than 0.01 eV/Å for force on every atom.

Supplementary Tables

Table S1. BET, pore size distribution and pore volume of samples

Sample	BET[a] $(m^2 \, g^{-1})$	Pore size distribution [b] (nm)	Pore volume [c] $(cm^3 \, g^{-1})$
KIT-6	744	5~13	1.16
KIT-6/Co_3O_4	417	5.5~7.5	0.63
M-Co_3O_4	144	2~5	0.21
M-Co_3O_{4-x} (205°C)	143.7	2~5	0.22
M-Co_3O_{4-x} (230°C)	129	2~5	0.204
M-Co_3O_{4-x} (250°C)	139	2~5	0.21
M-Co_3O_{4-x} (275°C)	130	2~7	0.234
M-Co_3O_{4-x} (300°C)	67	2-7	0.155
Co_3O_4	7	-	-
Co_3O_{4-x}	6.3	-	-

a: the Brunauer–Emmett–Teller (BET) method using the data in the relative pressure range of 0.05~0.15.

b: Pore size distributions (PSDs) were obtained from the adsorption isotherms using BJH mode.

c: The total pore volumes (V_{total}) were calculated from the N_2 adsorption amount at $P/P_0 = 0.995$.

Table S2. Comparison of electrochemical performance of reported Zn-ion batteries

Battery	Specific Capacity $(mAh \, g^{-1})$	Cycling performance	Ref.
Zn//M-Co_3O_{4-x}	420 mAh g^{-1} at 1 A g^{-1}	400% retention after 60000 cycles	This work
Zn//V_2O_5	224 mAh g^{-1} at 0.1 A g^{-1}	81.% retention after 30 cycles	12
Zn//Co_3O_4	168 mAh g^{-1} at 1 A g^{-1}	80% retention	7

		after 2000 cycles	
Zn//α-MnO$_2$	382.2 mAh g^{-1} at 0.3 A g^{-1}	94% retention after 3000 cycles	35
Zn//ZnMn$_2$O$_4$	150 mAh g^{-1} at 0.5 A g^{-1}	94% retention after 500 cycles	36
Zn//VS$_2$	190.3 mAh g^{-1} at 0.05 A g^{-1}	98.0% retention after 200 cycles	37
Zn//PANI-MnO$_2$	280 mAh g^{-1} at 0.2 A g^{-1}	40% retention after 5000 cycles	38
Zn//Co(III) rich-Co$_3$O$_4$	205 mAh g^{-1} at 0.5 A g^{-1}	92% retention after 5000 cycles	10
Zn//Na$_{1.1}$V$_3$O$_{7.9}$@rGO	220 mAh g^{-1} at 0.3 A g^{-1}	93% retention after100 cycles	39
Zn//Na$_{0.95}$MnO$_2$	60 mAh g^{-1} at 2C	92% retention after 1000 cycles	40
Zinc/Aluminum Ion Battery	94 mAh g^{-1} at 0.1 A g^{-1}	94% retention after 200 cycles	41
Zn//MnO$_2$	366.6 mAh g^{-1} at 0.74 A g^{-1}	83.7% retention after 300 cycles	46
Zn//NiO	155 mAh g^{-1} at 1 A g^{-1}	65% retention after 500 cycles	11
Zn//H$_2$V$_3$O$_8$ NW/graphene	394 mAh g^{-1} at 1/3C	87% retention after 500 cycles	47
Zn//Co$_3$O$_4$@NiO	182.6 mAh g^{-1} at 5 mA cm^{-2}	89% retention after 500 cycles	48
Zn//Ni	346 mAh g^{-1} at 5 A g^{-1}	88% retention after 5000 cycles	8
Zn//NiCo$_2$O$_4$	183.1 mAh g^{-1} at 1.6 A g^{-1}	82.7% retention after 3500 cycles	49

Supplementary Figures
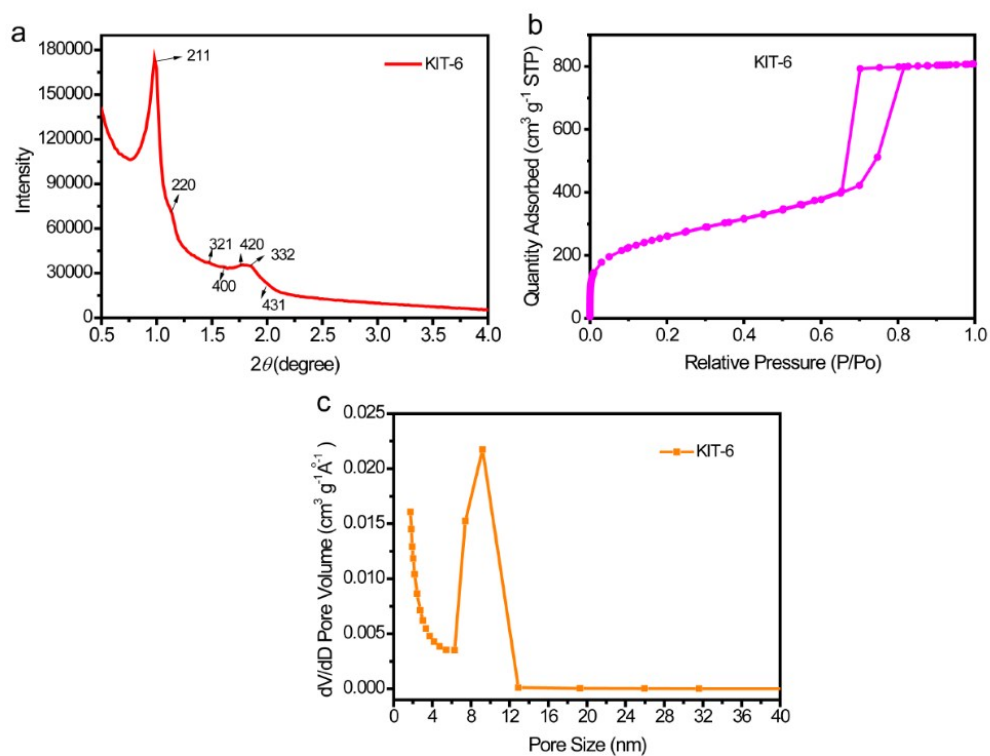
Fig. S1 XRD patterns, (c) N_2 sorption isotherms, (c) pore size distributions (PSDs) of hard template KIT-6.
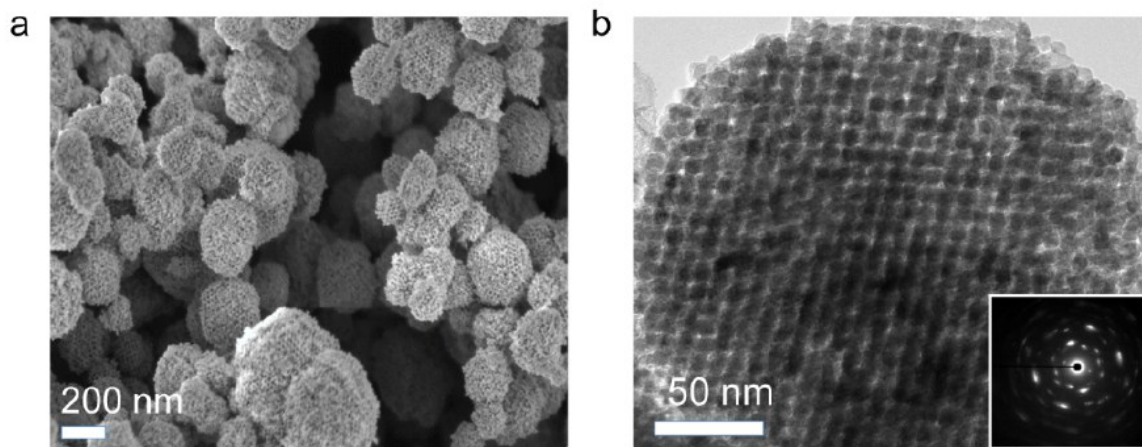

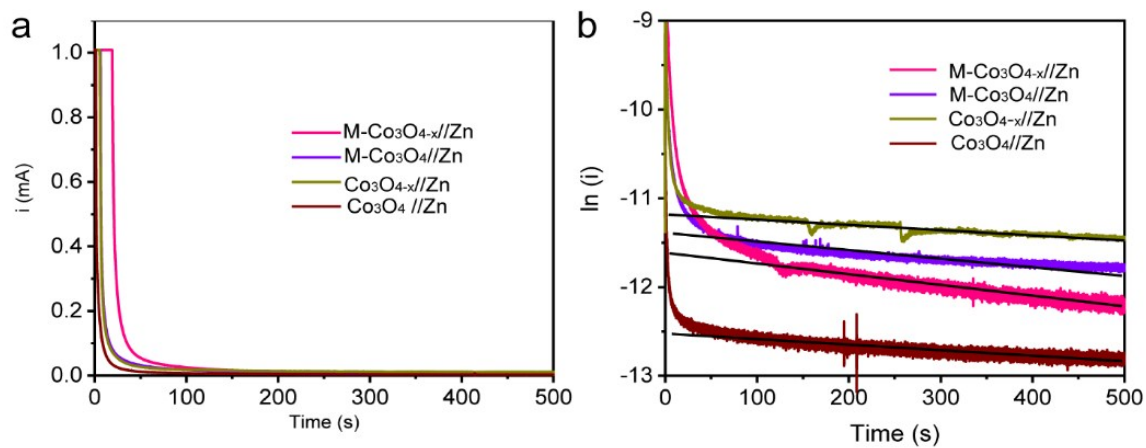
Fig. S2 (a) SEM and (b) TEM images of the M-Co_3O_4.
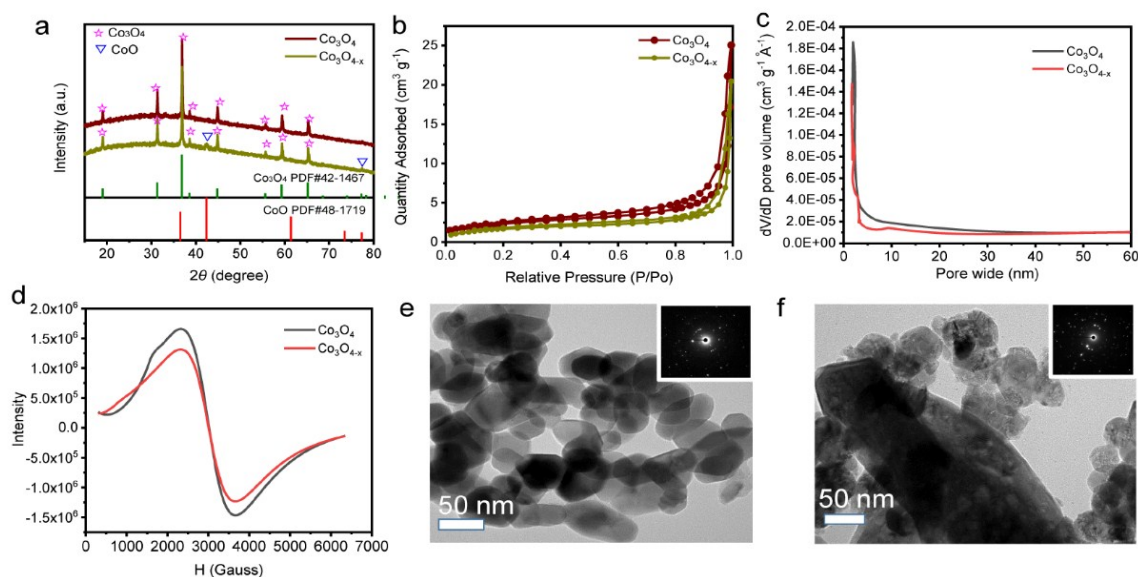
Fig. S3 The characterizations of no-porous Co_3O_4 and no-porous oxygen-vacancy Co_3O_{4-x}, (a) XRD, (b) N_2 sorption isotherms, (c) pore size distributions (PSDs), (d) EPR spectra and TEM images (e) Co_3O_4, (f) Co_3O_{4-x}.
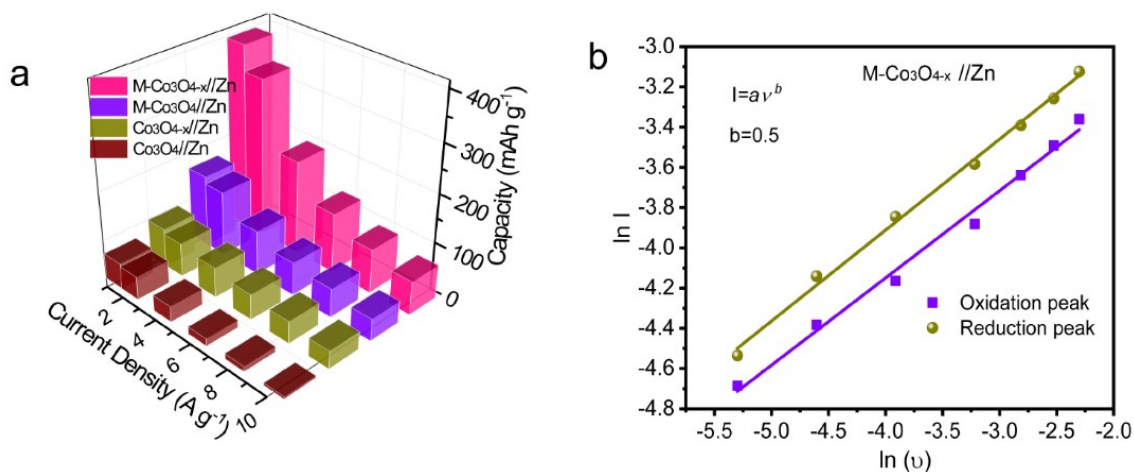

Fig. S4 (a) The capacity of M-Co_3O_{4-x}//Zn, M-Co_3O_4//Zn, Co_3O_{4-x}//Zn and Co_3O_4//Zn batteries at different current densities. (b) The relationship of redox peak currents with the scan rates for M-Co_3O_{4-x}//Zn battery.
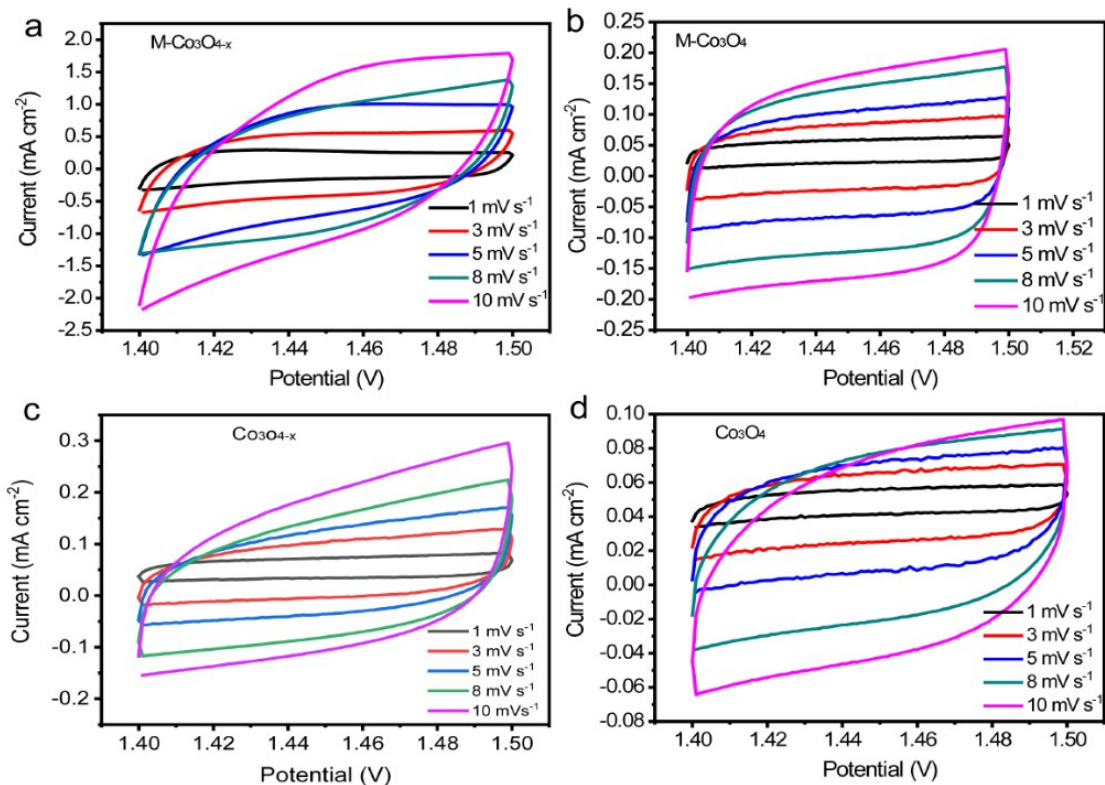
Fig. S5 Cyclic voltammogram curves were measured in a non-faradaic region of the voltammogram at the different scan rates.

Fig. S6 (a) Transient *i-t* curves of the M-Co_3O_{4-x}//Zn, M-Co_3O_4//Zn, Co_3O_{4-x}//Zn and Co_3O_4//Zn electrodes collected at 1.72 V, and (b) the corresponding semi-logarithmic plots.
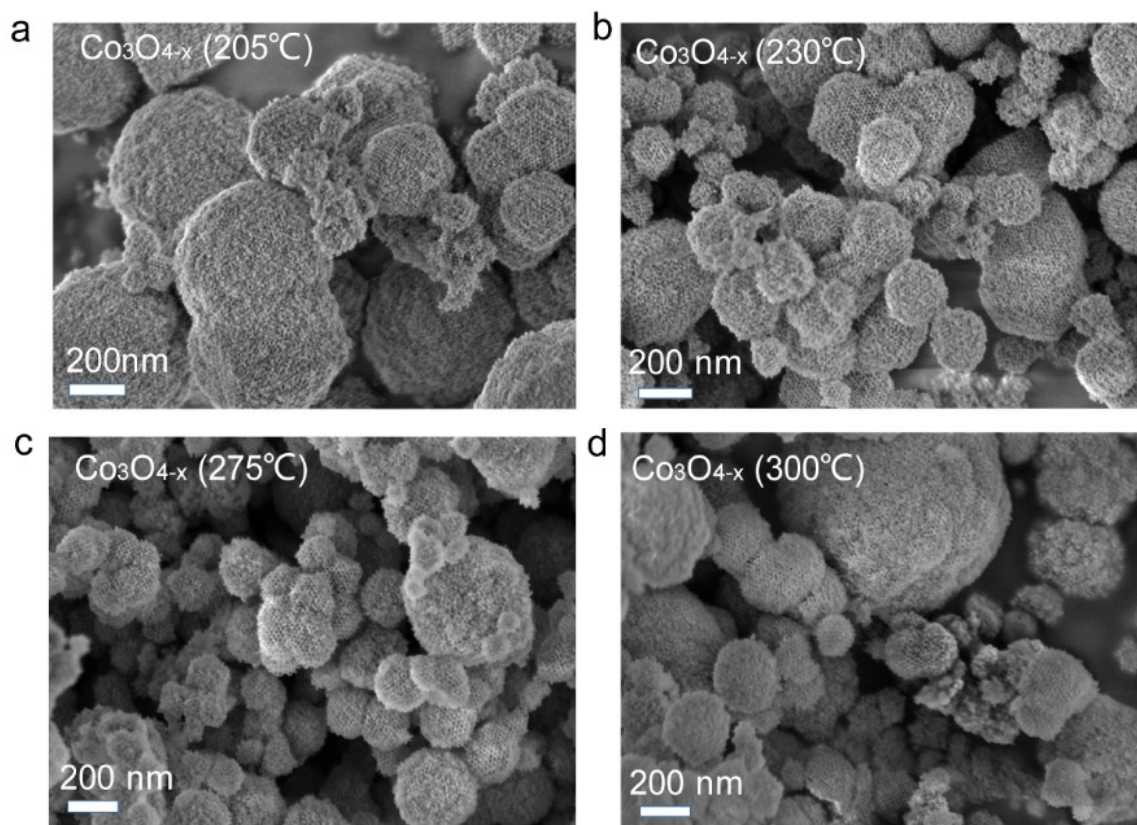
Fig. S7 SEM images of M-Co₃O₄₋ₓ (X) at different phosphating temperature.
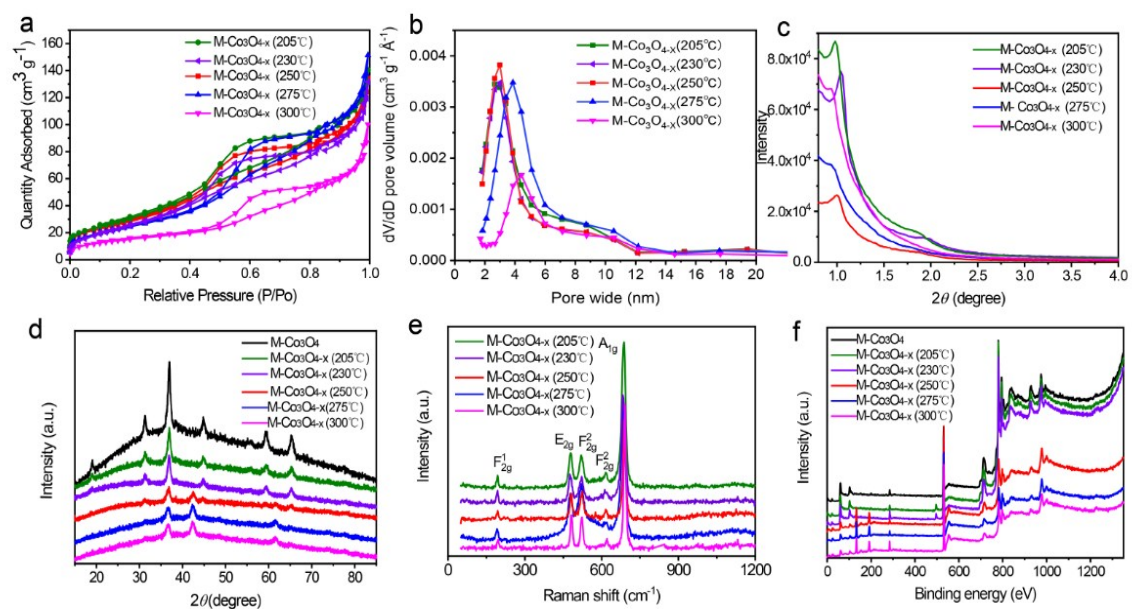
Fig. S8 The characterizations of M-Co$_3$O$_{4-x}$ (X) at different phosphating temperature, (a) N$_2$ sorption isotherms, (b) pore size distributions (PSDs), (c) (d) low-angle and wide-angle powder XRD, (e) Raman shift spectra and (f) XPS spectra.
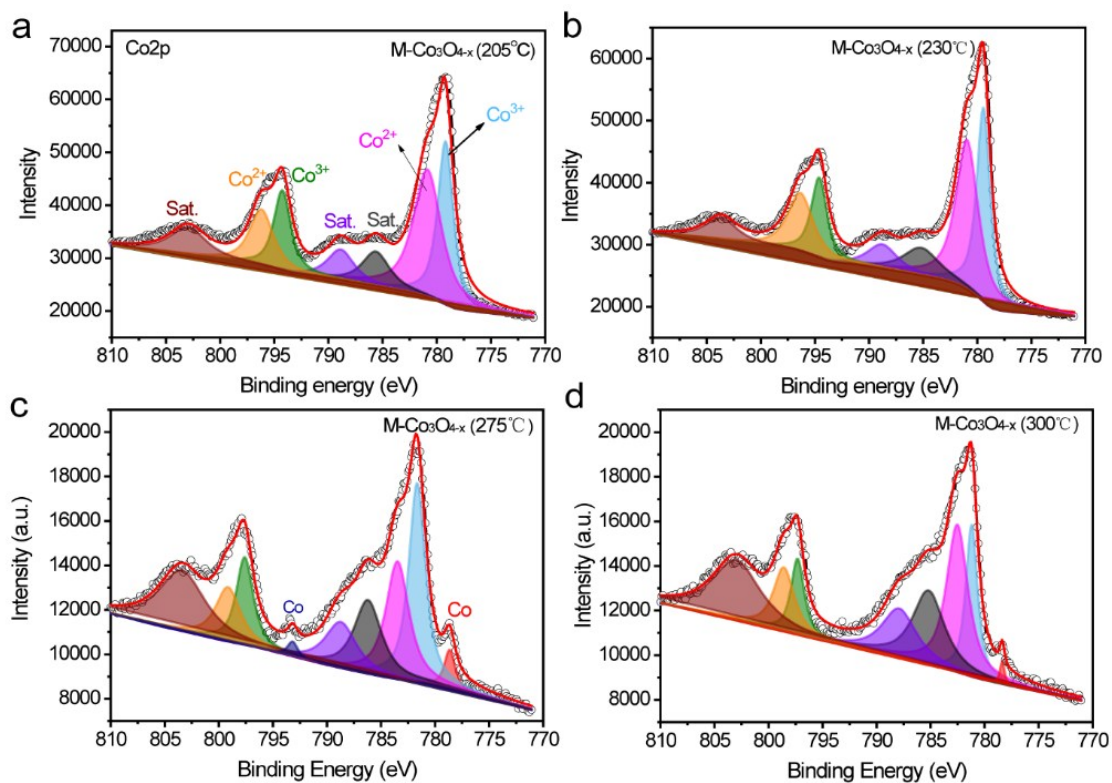
**Fig. S9** The high-resolution XPS spectra of Co 2p for M-Co$_3$O$_{4-x}$ (X) samples.
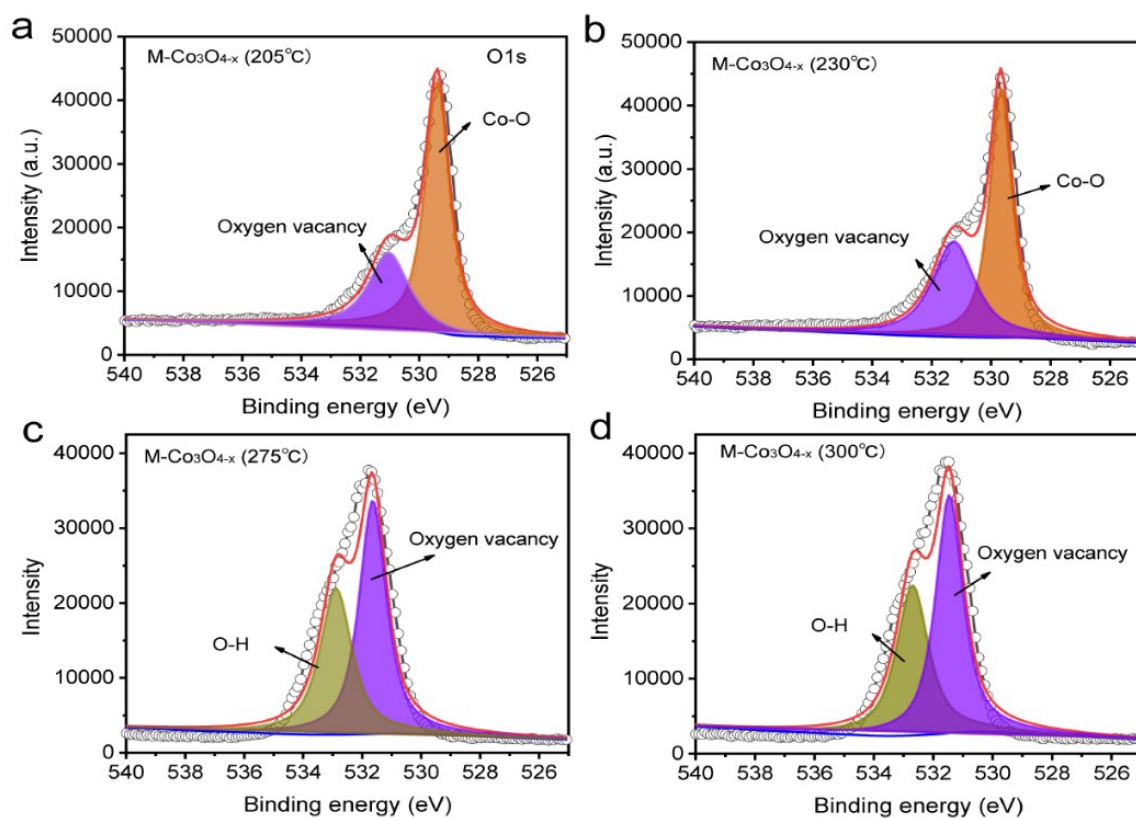
Fig. S10 The high-resolution XPS spectra of O 1s for M-Co$_3$O$_{4-x}$ (X) samples.
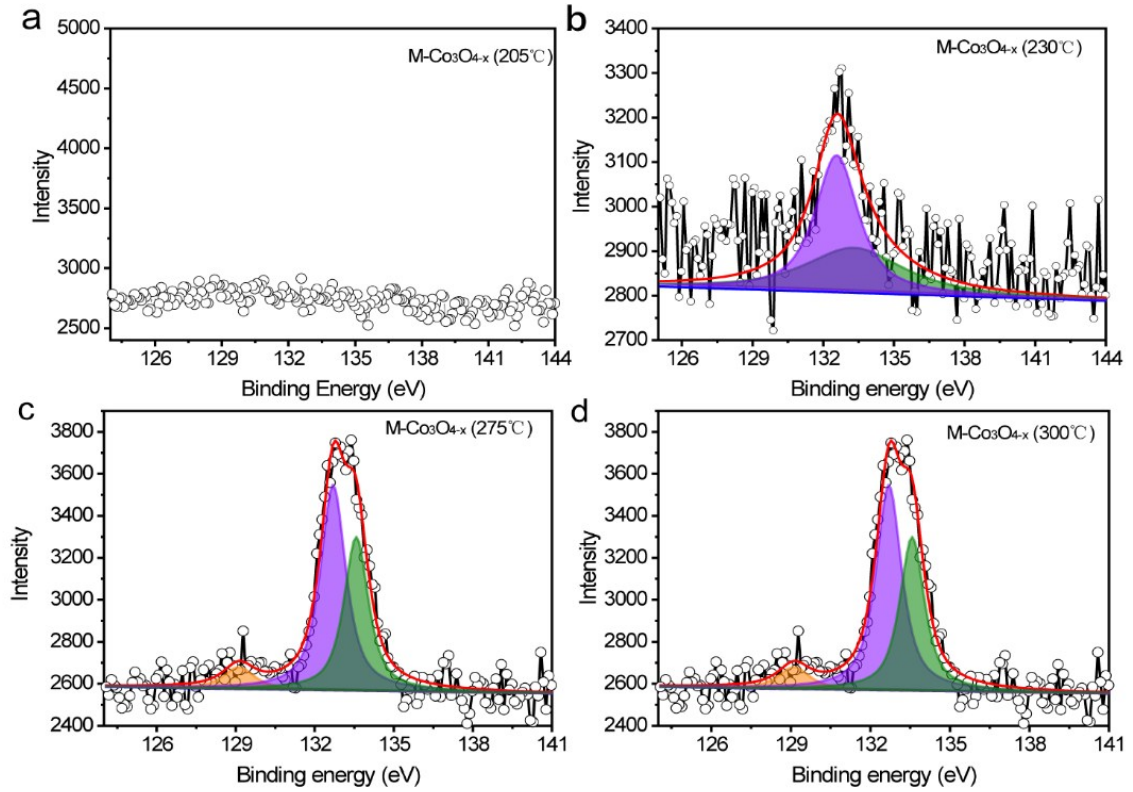
Fig. S11 The high-resolution XPS spectra of P 2p for M-Co$_3$O$_{4-x}$ (X) samples.
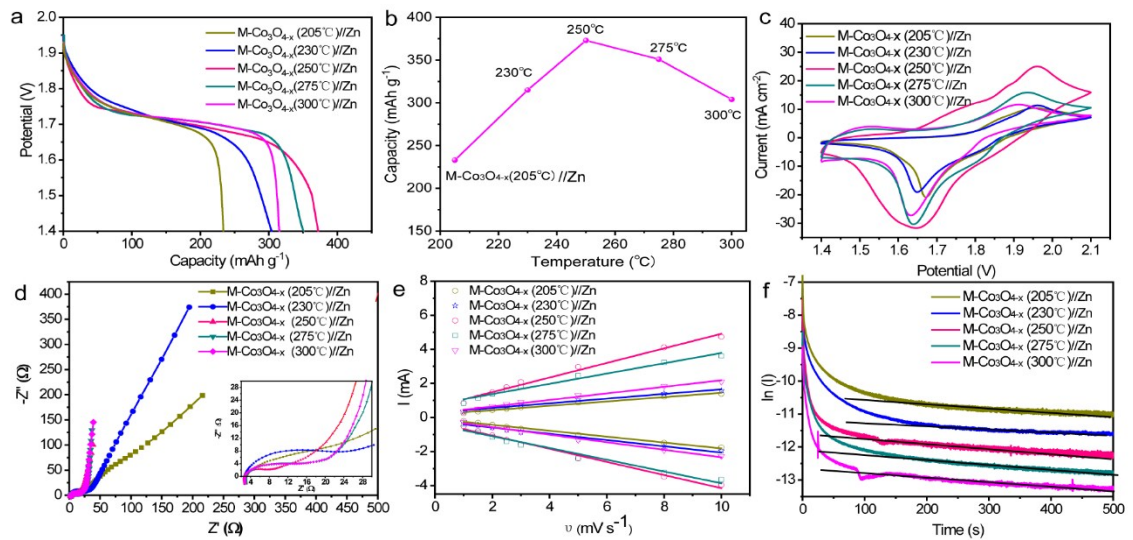

Fig. S12 The electrochemical performances of M-Co$_3$O$_{4-x}$ (X)//Zn batteries: (a) the discharge curves at 1 A g^{-1}. (b) The capacity of four batteries at 1 A g^{-1}. (c) CV curves at 10 mV s^{-1}. (d) EIS. (e) The fitted electrochemical double-layer capacitance C$_{dl}$ by the slope of $i_c = v\,C_{dl}$ at 1.45 V. (f) The semi-logarithmic plots of transient *i-t* curves of the M-Co$_3$O$_{4-x}$ (X) electrodes collected at 1.72 V.
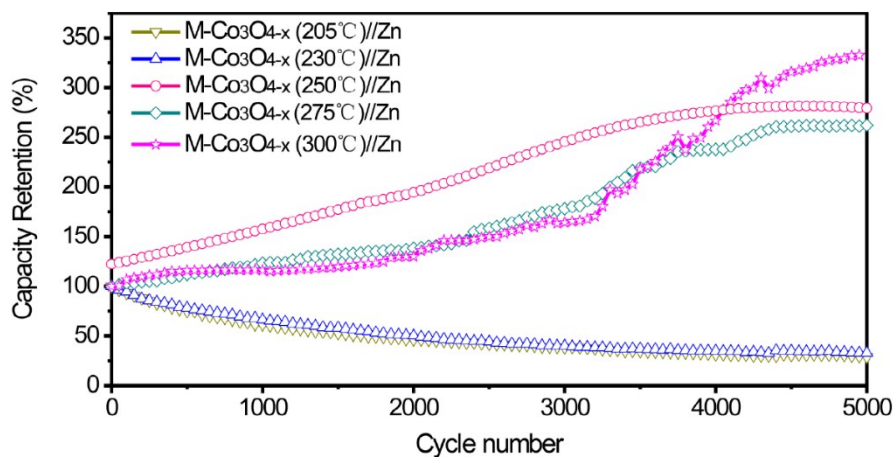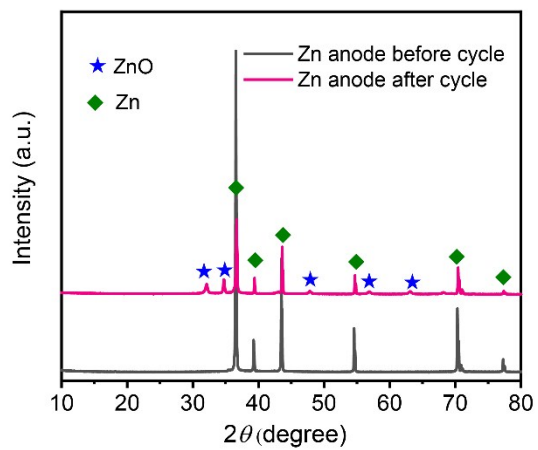
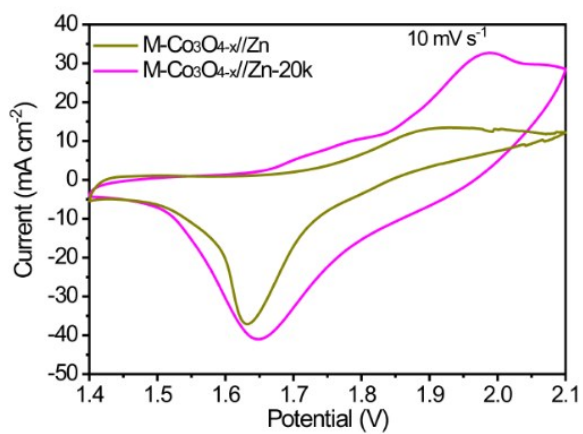**Fig. S13** Cycling performance of M-Co$_3$O$_{4-x}$ (X)//Zn batteries at 5 A g^{-1}.
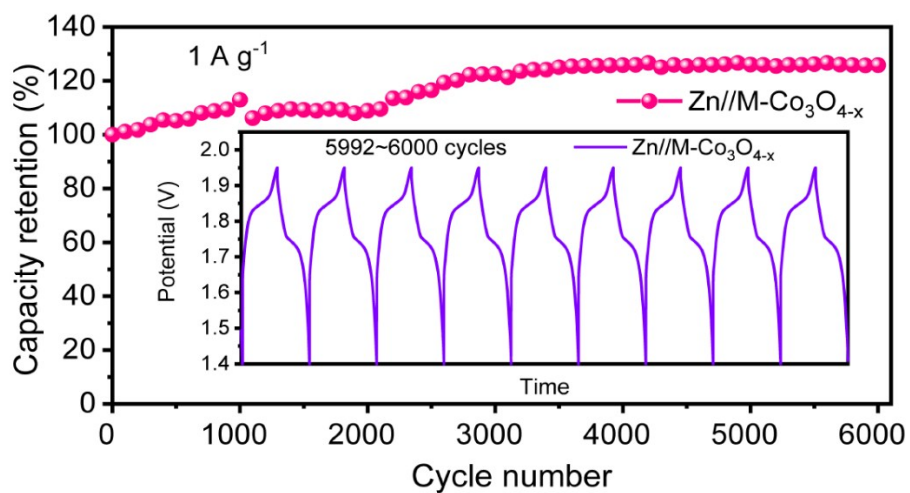
Fig. S14 Cycling performance of M-Co$_3$O$_{4-x}$ //Zn battery at 1 A g^{-1}.
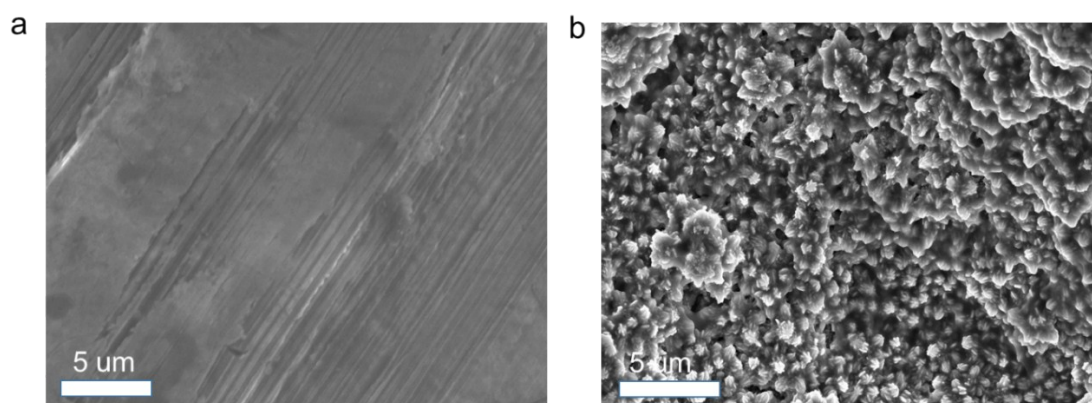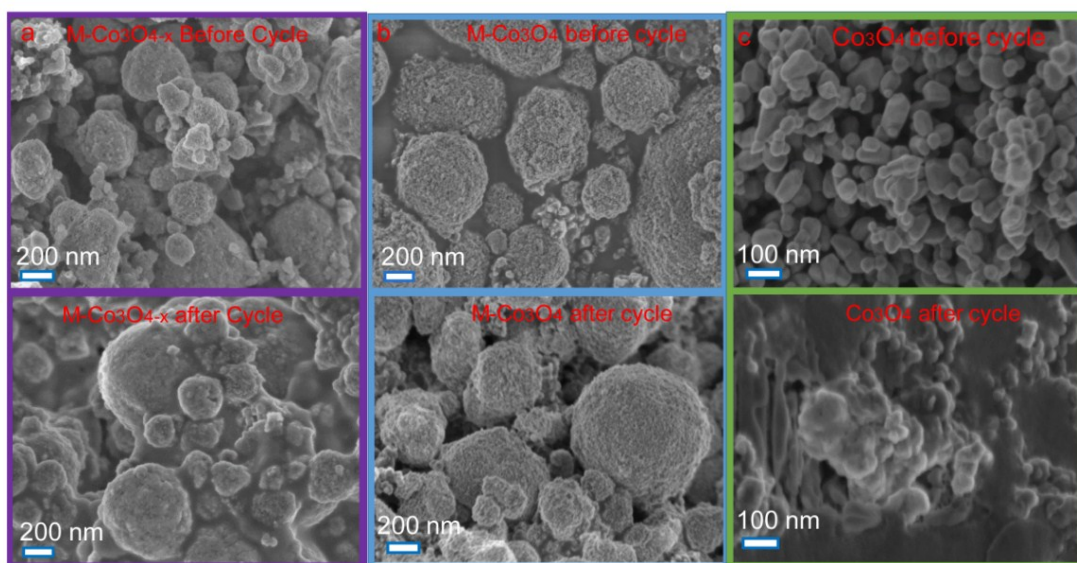

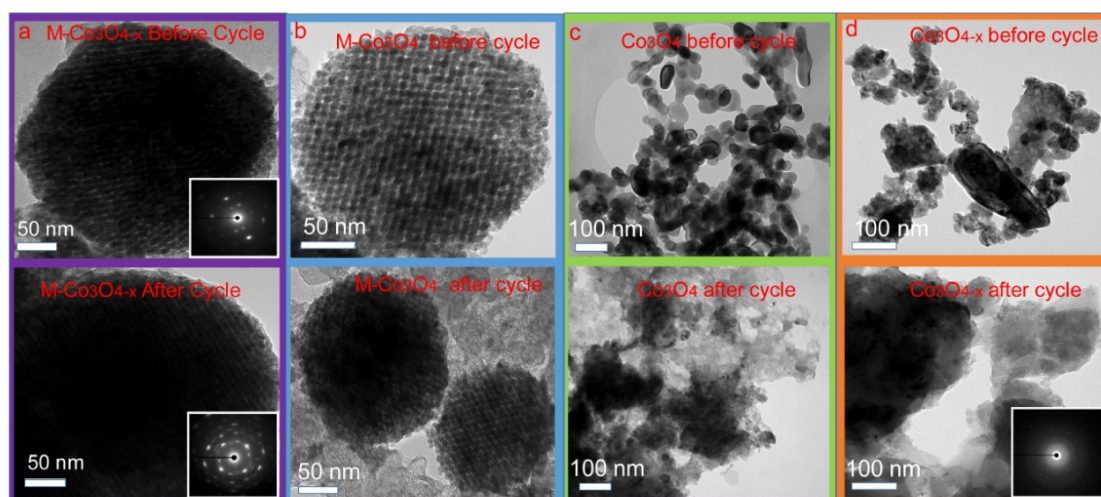
Fig. S15 The SEM images of Zn anode before (a) and after cycle (b).

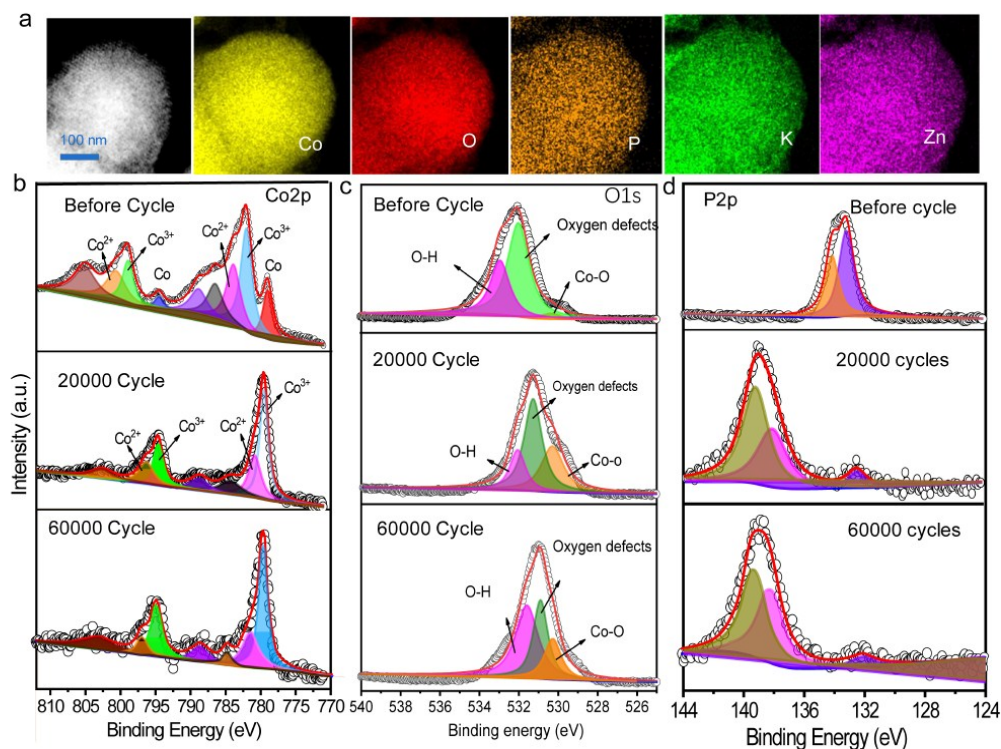**Fig. S16** The XRD patterns of Zn anode before and after cycle.

Fig. S17 The CV curves of M-Co$_3$O$_{4-x}$//Zn battery before and after 20000 cycles

**Fig. S18** The SEM images of M-Co$_3$O$_{4-x}$, M-Co$_3$O$_4$ and Co$_3$O$_4$ electrodes before and after cycles.

Fig. S19 The TEM images of M-Co$_3$O$_{4-x}$, M-Co$_3$O$_{4-x}$, Co$_3$O$_4$ and Co$_3$O$_{4-x}$ electrodes before and after cycles.

Fig. S20 (a) High-angle annular dark-field scanning TEM (HAADF-STEM) of M-Co$_3$O$_{4-x}$ electrode after cycles and its corresponding elementals color mapping. And their corresponding high-resolution XPS spectra of Co 2p (b), O 1s (c) and P 2p (d) peaks of before cycle, 20000 cycles and 60000 cycles.
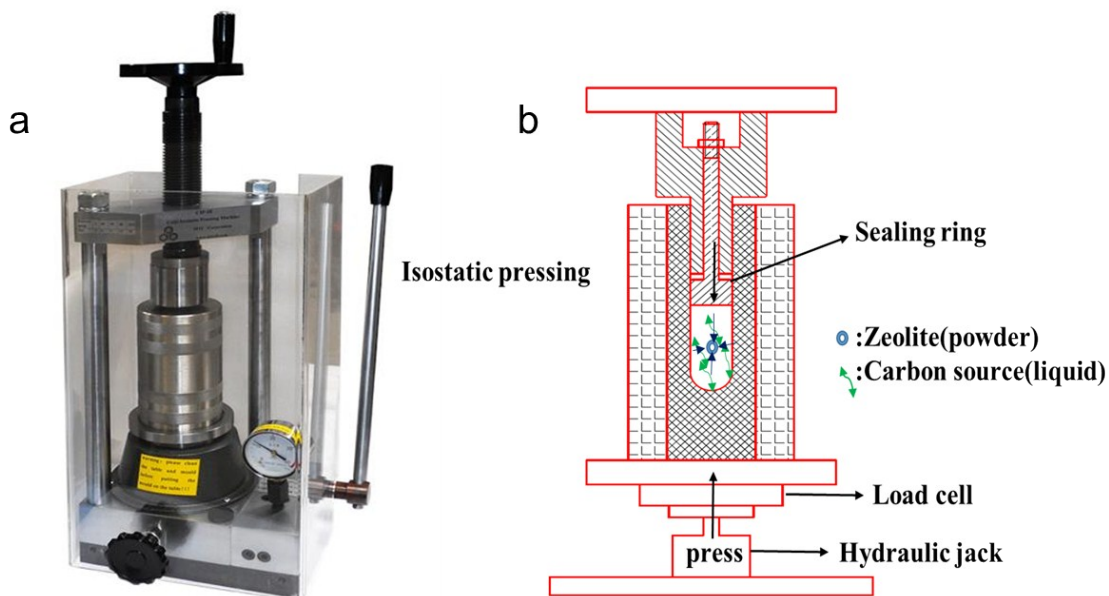
Fig. S21 (a) The picture of isostatic-pressing equipment, (b) the simple sketch of pressure cell.